Flexible Aircraft Gust Encounter Simulation using Subspace Projection Model Reduction

P. Bekemeyer and S. Timme*

School of Engineering, The University of Liverpool
The Quadrangle, L69 3GH Liverpool, United Kingdom

Abstract

Reduced-order modelling of multidisciplinary computational fluid dynamics can enable routine industrial gust load analysis. Key to the herein presented model reduction approach is that it modularly builds upon the widely accepted modal structural reduced-order model, where high-fidelity aerodynamics are simply projected onto the structural degrees-of-freedom, while opening a novel route to account for dominant modal aerodynamics in multidisciplinary edge-of-the-envelope flight physics. The influence of the flexible structure is captured by aeroelastic eigenmodes which originate in the structural equations. Such global aeroelastic modes for a large aircraft case with nearly 50 million degrees-of-freedom are computed for the first time using exact aerodynamics from computational fluid dynamics via the Schur complement method. The influence of atmospheric gusts is captured by modes from proper orthogonal decomposition applied to sinusoidal gust responses at discrete frequencies. Afterwards, the two sets of modes are combined and the linearised operator of the Reynolds-averaged Navier–Stokes equations coupled with a modal structural model is projected onto the resulting subspace. The constructed low-dimensional model can be solved rapidly for practical gust analysis giving accurate agreement with the full-order reference results throughout. Feasibility of aeroelastic model reduction, using the industry-grade computational fluid dynamics package DLR–TAU, for a relevant use case in transonic flight gust encounter is demonstrated.

Keywords: Gust analysis, Large aircraft, Computational fluid dynamics, Aeroelastic model reduction, Modal decomposition

*Corresponding author
Email address: sebastian.timme@liverpool.ac.uk (P. Bekemeyer and S. Timme)

NOMENCLATURE

A	=	Jacobian matrix
C_L	=	lift coefficient
c_p	=	pressure coefficient
I	=	identity matrix
L_g	=	gust length
L_{MAC}	=	mean aerodynamic chord
Q	=	matrix of oscillatory aerodynamic derivatives
$\boldsymbol{R}$	=	vector of non-linear residual functions
r	=	relative information content in proper orthogonal decomposition
S	=	snapshot matrix in proper orthogonal decomposition
S	=	Schur complement matrix
t	=	time
U_∞	=	freestream velocity
V	=	diagonal matrix containing cell volumes
$\boldsymbol{v}_g$	=	vector of gust disturbances
v_{gz}	=	vertical gust amplitude
$\boldsymbol{w}$	=	vector of conservative variables
$\boldsymbol{x}$	=	eigenvector in proper orthogonal decomposition
$\dot{\boldsymbol{x}}$	=	vector of grid point velocities
x_0	=	gust off-set distance
$\boldsymbol{z}$	=	vector of reduced space variables
ε	=	finite-difference step size
λ	=	eigenvalue in eigenmode decomposition
μ	=	eigenvalue in proper orthogonal decomposition
Φ, Ψ	=	basis for Petrov–Galerkin projection
$\boldsymbol{\phi}$	=	mode in proper orthogonal decomposition
$\boldsymbol{\phi}, \boldsymbol{\psi}$	=	right and left eigenvectors in eigenmode decomposition
ω	=	dimensionless reduced frequency

Subscripts

f	=	fluid
s	=	structure
EMD	=	eigenmode decomposition
POD	=	proper orthogonal decomposition

1. Introduction

Investigation of aircraft structural responses to atmospheric turbulence is an important part of aircraft design and certification since a few extreme gust load cases may be critical for wing sizing. Numerous parameters, e.g. flight point, mass case, gust shape and length, need to be investigated. Thus, low-cost methods which offer high-fidelity results within an affordable time frame are desired to ensure an accurate and reliable prediction of loads. Traditionally, linear potential aerodynamic theory in frequency domain, mostly the doublet lattice method [1], is used to obtain such loads rapidly. Examples for this are widespread from isolated wings [2] to full aircraft configurations [3]. While compressibility is accounted for, non-linear aerodynamic features, such as shock waves and boundary-layer separation, are neglected even though these are dominating the flow physics in transonic flight conditions where nearly all modern large aircraft operate. Two routes are commonly pursued to overcome this known lack of fidelity. Correction factors, either from experiment or computational fluid dynamics (CFD), can be applied after calculating forces from linear aerodynamic theory to improve predictions [4]. While this first route nearly retains the low computational effort of the underlying linear aerodynamic theory, correction factors using CFD are normally based on sampling at zero frequency only and an expertly selected set of modes, which inhibits a fully automated set-up due to the human in the loop. Nevertheless, correcting aerodynamic loads is current industrial standard. The second route is analysing responses using non-linear CFD integrated into a multidisciplinary toolset [5, 6], which can offer improved loads predictions also at transonic conditions. However,

computational cost of such general-purpose time-accurate simulations as part of industrial loads cycles remains prohibitive.

A promising, albeit not new, approach to reduced computational cost of CFD simulations, and thus to make such higher-fidelity tools affordable in the aircraft loads process, is reduced-order modelling (ROM) [7]. Different approaches have been proposed specifically for gust response analyses including the autoregressive moving average method [5] and proper orthogonal decomposition from time-marching snapshots combined with convolution [8] and system identification [9]. In contrast to previous work, we are specifically interested in the type of 'modal decomposition and subspace projection' methods. As one of those, structure-only model reduction based on projection with in-vacuum eigenmodes of the mass-spring system has been used for decades in aircraft loads and aeroelastics in combination with linear aerodynamics [10], while projection with eigenmodes has also gained interest within the fluid dynamics community [11]. Extracting eigenmodes from the operator describing higher-fidelity aerodynamic theory is non-trivial [12, 13]. With interest in coupled fluid-structure problems and using linear and non-linear potential flow models, e.g. [14, 15] presented aerodynamic ROMs with a basis of direct and adjoint eigenmodes for coupling with a structural model, which was later resuscitated in [16] using coupled aeroelastic eigensolutions directly for the projection. Turning towards higher-fidelity aerodynamics which are more suited for feature-rich and edge-of-the-envelope flow physics, and initially assuming interest in wind-off structural modes, the Schur complement method can be applied to track these eigenmodes while being affected by linearised CFD aerodynamics [17]. Critical eigenmodes of the coupled system can be used in a centre manifold reduction to investigate transonic aeroelastic limit-cycle oscillation and to perform parametric sensitivity analysis [18]. While excellent agreement between results from the underlying full-order non-linear system and ROM is observed for response to initial structural disturbance, results are not as satisfying during external forcing such as gust excitation [19]. More recently, the authors proposed a model extension to overcome this lack of accuracy by including additional modes representing the

gust response characteristics of the system [20].

Instead of attempting to extract global eigenmodes that properly describe gust behaviour, proper orthogonal decomposition (POD) is used [21]. POD was first used in fluid dynamics to model coherent structures in turbulent flow fields [22]. This common model reduction technique is based on subspace projection, too. It allows the creation of a reduced basis for problems of very large size because the system response is sampled rather than quizzing the eigenmode characteristics of the Jacobian matrix, which quickly becomes computationally prohibitive for industry relevant cases. A small eigenvalue problem, related to snapshots generated by numerically analysing the full system, is solved to obtain modes. This approach was soon extended towards frequency-domain sampling data from an incompressible three-dimensional vortex lattice method [23]. Linearised CFD aerodynamics were first considered to analyse the aeroelastic behaviour of a pitch-plunge aerofoil [24] and a three-dimensional wing [25]. Recently, an application to aeroelastic gust responses has been presented for an aerofoil in sub- and transonic flow conditions, showing excellent agreement at two orders of magnitude reduced computational cost [20]. Results have subsequently been presented for a large civil aircraft [26]. Closely related work can also be found in [27, 28]. Combining POD with a linearised frequency-domain method not only reduces computational cost further, but, more importantly, an interpolation for frequencies not pre-computed can be avoided.

The current paper consolidates these developments by enriching an eigenmode decomposition (EMD) ROM with POD modes to increase the prediction accuracy for loads occurring during transient gust encounter of a flexible large civil aircraft. Importantly, practical feasibility is demonstrated for such a test case of industrial relevance with an industry-grade CFD package solving the Reynolds-averaged Navier–Stokes (RANS) equations. The construction of the EMD ROM is first discussed and mode traces as well as global modes are analysed. The lack of accuracy for gust responses is demonstrated for a typical 1–cos gust scenario. A POD model of the aerodynamics is then introduced and the two modal sets are combined. Responses of the coupled ROM are compared with

full-order model simulations scrutinising integrated aerodynamic loads, surfaces pressures and structural deformations. Finally, computational cost for creating and solving the ROM is elucidated.

2. Theoretical Formulation

2.1. Introducing Linearised Dynamics

The coupled full-order non-linear system is first presented. The state-space vector $\boldsymbol{w}$ of dimension n can be written as

$$\boldsymbol{w} = \left[\boldsymbol{w}_{\mathrm{f}}^T, \boldsymbol{w}_{\mathrm{s}}^T\right]^T \tag{1}$$

where $\boldsymbol{w}_{\mathrm{f}}$ and $\boldsymbol{w}_{\mathrm{s}}$ denote fluid and structural degrees-of-freedom, respectively. While a typical dimension of $\boldsymbol{w}_{\mathrm{s}}$ is $\mathcal{O}(100)$ using a linear modal structural model, derived from a full finite-element discretisation of the structure, the fluid degrees-of-freedom can amount to very many millions. The governing equations in semi-discrete form are

$$\tfrac{\mathrm{d}}{\mathrm{d}t}(M\boldsymbol{w}) = \boldsymbol{R}(\boldsymbol{w}, \boldsymbol{v}_{\mathrm{g}}) \tag{2}$$

where $\boldsymbol{R}$ is the vector of non-linear residual functions corresponding to the unknowns $\boldsymbol{w}$, and $\boldsymbol{v}_{\mathrm{g}}$ denotes external disturbances due to gusts. The diagonal matrix M is partitioned just as the vector of unknowns and contains the cell volumes V for fluid degrees-of-freedom, since we apply an industry-standard finite-volume CFD method (specifically the DLR–TAU solver, cf. Section 3.1), and an identity matrix I for the structure. The difference between an equilibrium steady-state solution $\bar{\boldsymbol{w}}$ of Eq. (2) and the instantaneous state-space vector $\boldsymbol{w}$ is introduced as

$$\widetilde{\boldsymbol{w}} = \boldsymbol{w} - \bar{\boldsymbol{w}} \tag{3}$$

and accordingly for external disturbances $\boldsymbol{v}_{\mathrm{g}}$ and the cell-volume matrix V.

The residual in Eq. (2) is expressed around the equilibrium point by a first-order Taylor expansion assuming small disturbances

$$M\frac{\mathrm{d}\widetilde{\boldsymbol{w}}}{\mathrm{d}t} \approx \boldsymbol{R}(\bar{\boldsymbol{w}}, \bar{\boldsymbol{v}}_\mathrm{g}) + \frac{\partial \boldsymbol{R}}{\partial \boldsymbol{w}}\widetilde{\boldsymbol{w}} + \frac{\partial \boldsymbol{R}}{\partial \boldsymbol{v}_\mathrm{g}}\widetilde{\boldsymbol{v}}_\mathrm{g} \tag{4}$$

where $\boldsymbol{R}(\bar{\boldsymbol{w}}, \bar{\boldsymbol{v}}_\mathrm{g})$ represents the steady-state solution and is assumed to be zero without loss of generality due to enforced linearity. For ease of notation, the diagonal matrix at steady state is denoted M (and V for the corresponding cell-volume matrix) dropping the overbar $\bar{(\,)}$. The term $\partial \boldsymbol{R}/\partial \boldsymbol{w} = A$ denotes the coupled Jacobian matrix which is partitioned, too, as

$$A = \begin{bmatrix} A_\mathrm{ff} & A_\mathrm{fs} \\ A_\mathrm{sf} & A_\mathrm{ss} \end{bmatrix} \tag{5}$$

The meaning of the different sub-blocks has been discussed elsewhere [29], but shall be summarised for convenience. Blocks A_ff and A_fs, which require access to the spatial discretisation of the aerodynamic model including boundary conditions, describe the fluid Jacobian matrix and the influence of structural motion on the fluid, respectively. The second coupling block A_sf essentially involves the differentiation of the generalised forces, contained in the structural equations, with respect to the fluid unknowns, and A_ss is the structural Jacobian matrix, well known from structural dynamics, describing mass and stiffness properties. Matrix $\partial \boldsymbol{R}/\partial \boldsymbol{v}_g$ is used to introduce gust disturbances $\widetilde{\boldsymbol{v}}_g$ via artificial mesh velocities, following the widely applied field velocity method [30]. Since such gust definition does not directly act on the structural equations, but only through generalised aerodynamic forces, the structural part of the latter matrix ($\partial \boldsymbol{R}_s/\partial \boldsymbol{v}_g = 0$) is only required to keep consistent matrix/vector dimensions.

Note that the product of equilibrium solution and time rate of change of cell volumes, $\bar{\boldsymbol{w}}\frac{\mathrm{d}\widetilde{M}}{\mathrm{d}t}$, which is a by-product of dealing with finite-volume discretisations and respecting the geometric conservation law, is contained within the matrix block A_fs to simplify the notation [31]. This additional term only applies to the fluid equations and is irrelevant for the structural degrees-of-freedom.

2.2. Unified Modal Basis and Model Reduction

An aeroelastic ROM is introduced to investigate the influence of gust excitation on flexible structures by combining the individual bases of eigenmodes and POD modes, to be introduced below,

$$\Phi = [\Phi_{\mathrm{EMD}}\ ,\ \Phi_{\mathrm{POD}}] \quad \text{and} \quad \Psi = [\Psi_{\mathrm{EMD}}\ ,\ \Psi_{\mathrm{POD}}] \tag{6}$$

where $\Psi_{\mathrm{POD}} = \Phi_{\mathrm{POD}}$. Only the aerodynamic subsystem is considered to identify Φ_{POD} and thus all POD modes are padded with zero entries in the structural degrees-of-freedom of the coupled system. POD sampling which includes structural responses is possible (cf. [32] for solution of the coupled linearised equations) but shall not be discussed herein. Such a model reduction technique combining subspaces where each of them addresses a specific aspect of the coupled system enables the robust construction of a multi-purpose ROM.

Describing the change in state-space vector $\widetilde{\boldsymbol{w}}$ by

$$\widetilde{\boldsymbol{w}} = \Phi \boldsymbol{z} \tag{7}$$

where the complex-valued vector $\boldsymbol{z}$ describes the state-space variables in the reduced space (essentially the modal amplitudes), and substituting in Eq. (4), gives after performing a projection in the Petrov–Galerkin sense,

$$\Psi^H M \Phi \dot{\boldsymbol{z}} = \Psi^H A \Phi \boldsymbol{z} + \Psi^H \frac{\partial \boldsymbol{R}}{\partial \boldsymbol{v}_{\mathrm{g}}} \widetilde{\boldsymbol{v}}_{\mathrm{g}} \tag{8}$$

where $(\,)^H$ denotes Hermitian (conjugate) transpose and $\dot{(\,)}$ is the temporal derivative $\frac{\mathrm{d}()}{\mathrm{d}t}$. Since bi-orthonormality of the unified basis, in contrast to the individual bases, is no longer fulfilled for the coupled model, i.e. $\Psi^H M \Phi \neq I$, the inverse of $\Psi^H M \Phi$ is pre-multiplied resulting in the time-domain representation of the coupled reduced-order model

$$\dot{\boldsymbol{z}} = (\Psi^H M \Phi)^{-1} \Psi^H A \Phi \boldsymbol{z} + (\Psi^H M \Phi)^{-1} \Psi^H \frac{\partial \boldsymbol{R}}{\partial \boldsymbol{v}_{\mathrm{g}}} \widetilde{\boldsymbol{v}}_{\mathrm{g}} \tag{9}$$

While multiplying with the inverse changes the projection based on Ψ, the reduction described by $A\Phi$ remains unchanged. Solving the reduced system in either frequency (making the usual exponential function ansatz for $\boldsymbol{z}$) or time domain, and reconstructing full-order solutions afterwards, is an efficient way to investigate gust encounter for coupled fluid-structure systems.

2.3. Basis from Eigenmode Decomposition

Right and left eigenvectors, $\boldsymbol{\phi}_j$ and $\boldsymbol{\psi}_j$, of the coupled Jacobian matrix A are calculated by solving the direct and adjoint eigenvalue problems, respectively, corresponding to the homogeneous form of the linearised Eq. (4) (i.e. without gust forcing term),

$$\begin{aligned} \begin{bmatrix} A_{\mathrm{ff}} & A_{\mathrm{fs}} \\ A_{\mathrm{sf}} & A_{\mathrm{ss}} \end{bmatrix} \boldsymbol{\phi}_j &= \lambda_j M \boldsymbol{\phi}_j \quad \text{and} \\ \begin{bmatrix} A_{\mathrm{ff}}^T & A_{\mathrm{sf}}^T \\ A_{\mathrm{fs}}^T & A_{\mathrm{ss}}^T \end{bmatrix} \boldsymbol{\psi}_j^* &= \lambda_j M \boldsymbol{\psi}_j^* \quad \text{for} \quad j = 1, \ldots, m \end{aligned} \tag{10}$$

for which the number m is far smaller than the initial system size n while granting convergence of the numerical solution. The complex conjugate of the adjoint eigenvector $\boldsymbol{\psi}$ is denoted $\boldsymbol{\psi}^*$. The eigenvectors $\boldsymbol{\phi}$ and $\boldsymbol{\psi}$ (or $\boldsymbol{\psi}^*$ accordingly) are partitioned just as the state-space vector in fluid and structural components. The eigenvalue $\lambda_j = \sigma_j + i\omega_j$ describes the eigenmode's growth rate σ_j and reduced frequency ω_j, made non-dimensional using freestream velocity U_∞ and reference chord length L_{MAC} (where MAC is mean aerodynamic chord).

The Schur complement method is used to determine eigenmodes by tracking structural modes in a matched-point fashion while they are increasingly affected by the fluid with decreasing altitude. Specifically, interest is in eigenvalues emerging from the structural block A_{ss} (at high-altitude, effectively-uncoupled conditions), as aerodynamic stability is assumed [33][1], which allows the solution

[1] While the herein discussed gust response problem also assumes structural stability, this is not a requirement for the Schur complement method and structural instability is permissible in

of small non-linear eigenvalue problems, related to the structural degrees-of-freedom, for right and left structural eigenpairs, respectively,

$$S(\lambda_j)\boldsymbol{\phi}_{\mathrm{s},j} = \lambda_j \boldsymbol{\phi}_{\mathrm{s},j} \quad \text{and} \quad S^T(\lambda_j)\boldsymbol{\psi}^*_{\mathrm{s},j} = \lambda_j \boldsymbol{\psi}^*_{\mathrm{s},j} \quad \text{for} \quad j = 1, \ldots, m \tag{11}$$

where the matrix $S(\lambda_j)$ is the Schur complement of A_{ff} in A,

$$S(\lambda_j) = A_{\mathrm{ss}} - A_{\mathrm{sf}}(A_{\mathrm{ff}} - \lambda_j V)^{-1} A_{\mathrm{fs}} \tag{12}$$

Different levels of approximation have previously been proposed to decrease computational cost using CFD aerodynamics. All of them approximate the aerodynamic influence term, $A_{\mathrm{sf}}(A_{\mathrm{ff}} - \lambda_j V)^{-1} A_{\mathrm{fs}}$, solely describing the aerodynamic response due to the structural motion which is then projected onto the structural degrees-of-freedom. An extension to external forcing via gust responses, similar to traditional loads analysis with linear aerodynamic theory [34], is possible but shall not be discussed herein. The most simplistic way is to use the linearised frequency-domain incarnation of the discretised RANS operator and to sample the aerodynamic influence using a purely imaginary shift only, i.e. $\Im(\lambda_j) = \omega_j$,

$$A_{\mathrm{sf}}(A_{\mathrm{ff}} - \lambda_j V)^{-1} A_{\mathrm{fs}} \approx Q(\omega_j) = A_{\mathrm{sf}}(A_{\mathrm{ff}} - i\omega_j V)^{-1} A_{\mathrm{fs}} \tag{13}$$

Evaluation for all modes in an offline pre-computation step requires solutions of large (corresponding to the dimension of the fluid system), but sparse linear systems of equations for the columns in matrix A_{fs} as right-hand side. The direct and adjoint systems in Eq. (11) become

$$\begin{aligned} \big(A_{\mathrm{ss}} - Q(\omega_j)\big)\boldsymbol{\phi}_{\mathrm{s},j} &= \lambda_j \boldsymbol{\phi}_{\mathrm{s},j} \quad \text{and} \\ \big(A_{\mathrm{ss}} - Q(\omega_j)\big)^T \boldsymbol{\psi}^*_{\mathrm{s},j} &= \lambda_j \boldsymbol{\psi}^*_{\mathrm{s},j} \quad \text{for} \quad j = 1, \ldots, m \end{aligned} \tag{14}$$

general. Irrespective of the Schur complement method, the eigenmode basis can in principle be adapted to deal with dominant (i.e. weakly damped or unstable) global aerodynamic modes, but this discussion is beyond the scope of this work.

Newton's method is chosen to solve Eq. (14) at each altitude using either wind-off structural frequencies initially or the solution at a previous altitude as initial guess to the eigenvalue [17]. The eigenvector can be initialised randomly or for the wind-off structural system. We use the International Standard Atmosphere model to calculate density and velocity (via Mach number and speed of sound) at a defined altitude, required for the coupling between fluid and structural systems via the generalised force terms contained in matrix A_{sf}. Note that, as a simplification to ease computational cost, the aircraft's elastically trimmed shape at the target altitude is frozen, whereas the generalisation is easily possible conceptually and expensive numerically. During the Newton and altitude iterations, a Kriging surrogate model, as presented in [35], is used to interpolate between the pre-computed samples of $Q(\omega_j)$ rather than solving the full aerodynamic system in Eq. (13) in the loop.

This approach is closely related to pk-style flutter stability analysis [36]. For flutter stability analysis, normally both the crossing of an eigenvalue with the imaginary axis and weakly damped modes are of interest and thus the assumption of neglecting a damped oscillation during sampling is well justified and established for decades using linear aerodynamic theory. Similar to the classical p method for flutter investigation also a damped shift can be used for pre-sampling [37]. The impact of a pk-type assumption will be investigated below (cf. Figs. 5 and 7); while results for our flexible but fixed-in-space aircraft indicate that a standard pk-type approach is justified, other test cases which e.g. add flight dynamics modes to the analysis or have very low wing-bending frequencies (or both and hence the coupling becomes of interest) will have to be scrutinised more thoroughly concerning these approximations [38].

The fluid part of a coupled eigensolution requires additional solves of the corresponding expressions for direct and adjoint formulations, derived from the first row in Eq. (10),

$$\begin{aligned} (A_{\mathrm{ff}} - \lambda_j V)\boldsymbol{\phi}_{\mathrm{f},j} &= -A_{\mathrm{fs}}\boldsymbol{\phi}_{\mathrm{s},j} \quad \text{and} \\ (A_{\mathrm{ff}}^T - \lambda_j V)\boldsymbol{\psi}_{\mathrm{f},j}^* &= -A_{\mathrm{sf}}^T\boldsymbol{\psi}_{\mathrm{s},j}^* \quad \text{for} \quad j = 1, \ldots, m \end{aligned} \tag{15}$$

which adds $2m$ linear equation solves per modal basis. More detail of the various methods and approximations can be found in previous work [17, 19, 29, 35].

Collecting the eigenvectors, the right and left modal bases are formed as

$$\begin{aligned} \Phi_{\mathrm{EMD}} &= \left[\boldsymbol{\phi}_1, \ldots, \boldsymbol{\phi}_m, \boldsymbol{\phi}_1^*, \ldots, \boldsymbol{\phi}_m^*\right] \quad \text{and} \\ \Psi_{\mathrm{EMD}} &= \left[\boldsymbol{\psi}_1, \ldots, \boldsymbol{\psi}_m, \boldsymbol{\psi}_1^*, \ldots, \boldsymbol{\psi}_m^*\right] \end{aligned} \tag{16}$$

Note that aeroelastic eigensolutions originating in the wind-off structural modes appear as complex conjugate pairs and these complex conjugates are added to the modal basis at no additional cost. Eigenvectors are normalised to fulfil the bi-orthonormality condition

$$\Psi_{\mathrm{EMD}}^H M \Phi_{\mathrm{EMD}} = I \tag{17}$$

2.4. Basis from Proper Orthogonal Decomposition

We follow the method of snapshots to calculate a basis of POD modes. First, k snapshots of the entire flow field response due to gust forcing are computed by solving the linear system of equations corresponding to the linearised non-homogeneous form of Eq. (4) at discrete reduced frequencies ω_j,

$$\left(A_{\mathrm{ff}} - i\omega_j V\right) \widehat{\boldsymbol{w}}_{\mathrm{f},j} = -\frac{\partial \boldsymbol{R}_{\mathrm{f}}}{\partial \boldsymbol{v}_{\mathrm{g}}} \widehat{\boldsymbol{v}}_{\mathrm{g}}(\omega_j) \quad \text{for} \quad j = 1, \ldots, k \tag{18}$$

with $\widehat{\boldsymbol{w}}$ and $\widehat{\boldsymbol{v}}$ as complex-valued Fourier coefficients, assuming that $\widetilde{\boldsymbol{w}}$ and $\widetilde{\boldsymbol{v}}_{\mathrm{g}}$ in Eq. (4) change harmonically in time [39]. Solutions $\widehat{\boldsymbol{w}}_{\mathrm{f}}$ and their complex conjugates are stored as columns in the snapshot matrix S as

$$S = \left[\widehat{\boldsymbol{w}}_{\mathrm{f},1}, \ldots, \widehat{\boldsymbol{w}}_{\mathrm{f},k}, \widehat{\boldsymbol{w}}_{\mathrm{f},1}^*, \ldots, \widehat{\boldsymbol{w}}_{\mathrm{f},k}^*\right] \tag{19}$$

The POD basis Φ_{POD} is then obtained as a linear combination of snapshots

$$\Phi_{\mathrm{POD}} = SX \tag{20}$$

where eigenvector columns $\boldsymbol{x}_j$ in matrix X are scaled so that $\Phi_{\mathrm{POD}}^H V \Phi_{\mathrm{POD}} = I$. The eigenvalue problem of size $2k$

$$(S^H V S)\boldsymbol{x}_j = \mu_j \boldsymbol{x}_j \quad j = 1, \ldots, 2k \tag{21}$$

is solved to ensure the best possible approximation in Eq. (20). Eigenvalues μ_j are real and positive because $S^H V S$ is a Hermitian positive-definite matrix. The relative information content r_j contributed to the system by a certain mode, also often referred to as energy, is given by

$$r_j = \mu_j \cdot \left(\sum_{i=0}^{2k} \mu_i \right)^{-1} \quad \text{for} \quad j = 1, \ldots, 2k \tag{22}$$

This expression can be used to decrease the number of POD modes further by only considering those with a high relative information content, the ranking of which is driven by the gust forcing on the rigid aircraft.

Note that the dot product has been altered by weighting with the matrix of fluid cell volumes V. Whereas the robustness of the previously introduced EMD ROM is unaffected by this change in dot product, i.e. it is unconditionally stable, the characteristics of the POD model can change dramatically. First, cells with a small volume are becoming less important resulting in a more global flowfield representation. Secondly and more importantly, the resulting POD model is more likely to be stable compared with the case which excludes V, i.e. $S^H S$. The fact that stability of the POD ROM from Galerkin projection cannot be guaranteed, despite its popularity, has previously been discussed in [40] suggesting best practice based on numerical empiricism. Besides an appropriate weighting, another avenue to produce a stable ROM, following projection in the Petrov–Galerkin sense, is to adopt the balanced incarnation of POD [41].

3. Numerical Approach

3.1. Multidisciplinary Simulation Methods

Aerodynamics are simulated using the DLR–TAU code which is widely used in the European aerospace sector and validation of the code is available in the literature for steady [42, 43] and unsteady cases [43, 44]. The RANS equations in conjunction with the Spalart–Allmaras turbulence model [45] are solved. Inviscid fluxes are discretised applying a central scheme with the scalar artificial dissipation of Jameson, Schmidt and Turkel [46]. Exact gradients used for viscous and source terms are computed using the Green–Gauss approach [47]. Steady-state solutions are obtained using the backward Euler method with lower-upper Symmetric–Gauss–Seidel iterations and local time-stepping. Convergence is further accelerated by applying a V multigrid cycle on two grid levels [47].

Structural deformations are consistently considered using a linear modal approach. Mode shapes are calculated from a finite-element discretisation of the chosen configuration, and these modes are splined onto the point distribution of the CFD surface mesh to enforce the wing deformation in the coupled simulation and to obtain generalised forces integrated over the surface vice versa. Resulting volume-mesh deformations are calculated with the radial basis function method [48]. Gusts are modelled using the field velocity approach which introduces an artificial mesh velocity [30]. The velocity term is added to the fluxes in the governing equations and is prescribed based on the gust excitation while no additional deformation of the computational grid is required. The discrete geometric conservation law is fully accounted for. Previous studies have shown that the field velocity method, although the gust field is assumed to be frozen without being altered by the presence of the aircraft, is sufficiently accurate, compared with the far more expensive resolved gust approach, even for gusts as short as the reference chord length [49]. The relevant parameters for a typical 1–cos gust are visualised in Fig. 1.

During full-order unsteady simulations, aerodynamic and structural systems are solved alongside each other and data is exchanged on a subiteration level [50].

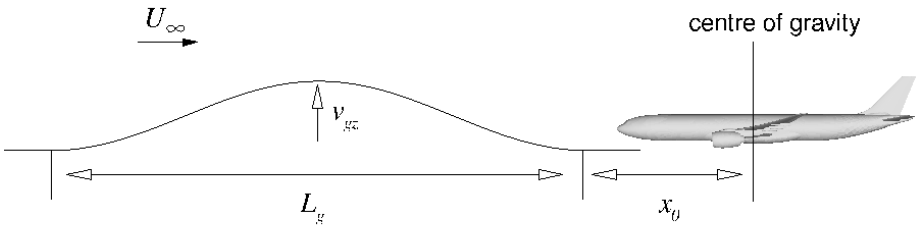

Figure 1: Sketch of 1–cos gust parameters.

Subiterations at each physical time step are performed until the Euclidean norm of the generalised-force update vector drops below 10^{-4} or a maximum number of 5 subiterations with data exchange between fluid and structure is reached. For the aerodynamic system a dual time-stepping combined with the second-order backward differentiation formula is used within subiterations, settings of which are summarised in Table 1. Chosen time-step size and number of time steps follow from numerical experiments and result as a trade-off between computational cost (runtime) and iterative error. A Cauchy convergence criterion with a tolerance of 10^{-8} for the relative error of the drag coefficient is applied in addition to a convergence criterion based on the density residual norm. The structural system is integrated in time applying the Newmark-beta method [51].

The linearised frequency-domain code follows a first-discretise-then-linearise, matrix-forming approach with an analytical, hand-differentiated fluid Jacobian matrix A_{ff}. Details of the implementation in the CFD solver, including the hand-differentiation of the chosen turbulence model, are provided in [31, 52, 53]. Matrix block A_{fs} uses a simple central finite-difference formulation generating one matrix column (corresponding to a structural mode) at a time, while a more recent addition to the code would also provide hand-differentiated Jacobian matrices related to the grid metrics [53]. Matrix A_{sf} is calculated analytically, too, for the pressure components of the generalised forces only, and A_{ss} is trivial due to the modal structural model. The matrix for the gust excitation on the right-hand side in Eq. (18) is discussed in more detail below. A generalised conjugate residual solver with deflated restarting is used to solve arising linear

Parameter	Value
Number of time steps	1500
Non-dimensional time-step size	0.1
Maximum number of subiterations per physical time step	5
Convergence criterion on force-update vector norm	10^{-4}
Convergence criterion on density residual norm	10^{-3}
Relative Cauchy convergence criterion on drag coefficient	10^{-8}

Table 1: Full-order time-domain numerical parameters

Parameter	Value
Number of Krylov vectors	80
Number of deflation vectors	20
Convergence criterion on residual of Krylov method	10^{-7}

Table 2: Frequency-domain numerical parameters

systems [54]. For preconditioning a block incomplete lower-upper factorisation of the Jacobian matrix with zero level of fill-in is selected [55, 56]. The number of Krylov and deflation vectors employed to solve linear systems together with the linear convergence criterion are given in Table 2 and the parameter selection is based on previously published results [54].

3.2. Implementation Details

Exploiting the concept of graph colouring [56], which has previously been applied in a similar context for evaluating the fluid Jacobian and Hessian matrices [57], the matrix block $\partial \boldsymbol{R}_f / \partial \boldsymbol{v}_\mathrm{g}$ in Eq. (9) is calculated explicitly (and stored) using sweeps of central finite-difference residual evaluations of the general form

$$-\frac{\partial \boldsymbol{R}_f}{\partial \boldsymbol{v}_\mathrm{g}} = \frac{\partial \boldsymbol{R}_f}{\partial \dot{\boldsymbol{x}}} = \frac{\boldsymbol{R}_f(+\varepsilon \dot{\boldsymbol{x}}) - \boldsymbol{R}_f(-\varepsilon \dot{\boldsymbol{x}})}{2\varepsilon} \tag{23}$$

which exploits the relation between mesh velocities and gust disturbance velocities [39], specifically $\dot{\boldsymbol{x}} = -\boldsymbol{v}_\mathrm{g}$. Computational cost is reduced by disturbing grid-point velocities $\dot{\boldsymbol{x}}$ of all points that are neither first nor second neighbour of a point in the stencil of another disturbed point. The set of disturbed points defines the columns of the matrix, while the resulting non-zero residual entries

define the rows. Following a first finite-difference evaluation, a new set of, as yet undisturbed, grid points is selected. This procedure is repeated until all points have been traversed once. Depending on mesh connectivity and partitioning applied, $\mathcal{O}(200)$ finite-difference evaluations are typically required for our test case to build the full matrix. In the absence of an analytical or automatic differentiation for this specific task, the finite-difference sweeps, implemented in the chosen flow solver for this purpose, to construct the full matrix $\partial \boldsymbol{R}_f / \partial \boldsymbol{v}_\mathrm{g}$ enables response simulations to arbitrary gust inputs.

Since a linear Taylor expansion is used, the assumption of a dynamically linear response also extends to integrated quantities, such as lift and moment coefficient. Thus, changes in global coefficients, e.g. lift coefficient $\widetilde{C}_L$, can be computed by forming the partial derivative $\partial C_L / \partial \boldsymbol{w}$ using steady-state information only and then substituting using Eq. (7),

$$\widetilde{C}_L = \frac{\partial C_L}{\partial \boldsymbol{w}} \widetilde{\boldsymbol{w}} = \frac{\partial C_L}{\partial \boldsymbol{w}} \boldsymbol{\Phi} \boldsymbol{z} \tag{24}$$

This enables the analysis of global coefficients without the need of reconstructing the surface solution from the ROM data, even though this can be done easily. Note that this formulation accounts for changes in integrated global coefficients due to aerodynamic as well as structural perturbations.

4. Results

The chosen test case is the large civil aircraft configuration XRF1, a three-view illustration of which is offered in Fig. 2. The XRF1 research test case is used by Airbus to engage with external partners on development and demonstration of relevant capabilities. XRF1 is an industrial standard multidisciplinary research test case representing a typical configuration for a long-range, wide-body aircraft. As such it features a total mass of about 200,000 kg and a fuselage length-to-diameter ratio of about 11. Consistent with the figure, the wing has approximate planform parameters as follows; an aspect ratio of about 8.5, a taper ratio of 0.22 and a 30° quarter-chord sweep angle. The MAC of the model

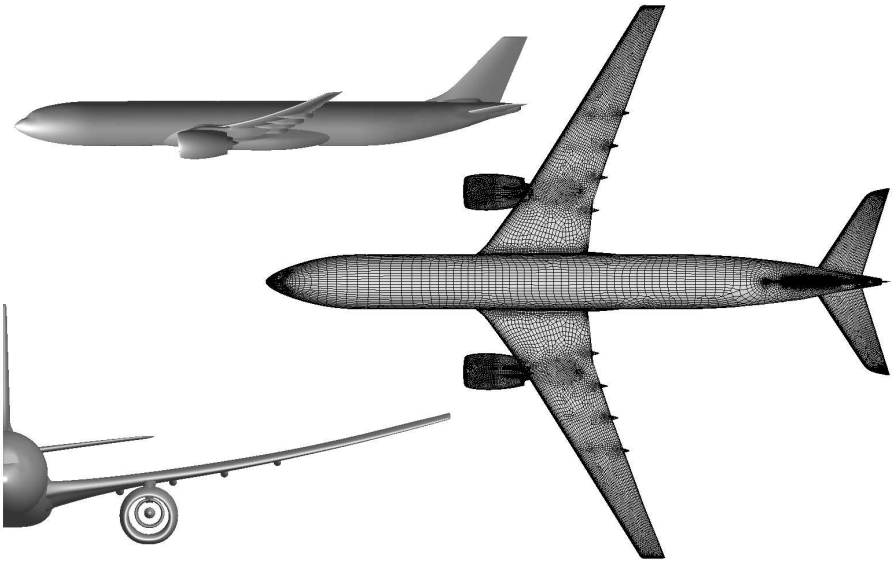

Figure 2: Three-view illustration of XRF1 aircraft configuration with surface-mesh detail.

is approximately 7.5 m with a span and reference area of 57 m and 380 m^2, respectively. Engine nacelles are treated as flow-through. While structural damping is not included in the analysis, structural mode shapes and frequencies are calculated from a global finite-element model of the configuration. The first wing-bending structural mode, multiplied by a scaling factor for enhanced visualisation, is shown in Fig. 3(a) together with the undeformed surface. While rigid-body dynamics are excluded in the present study, altogether 94 modes of the flexible structure are considered for static trimming, to be described below, and 15 modes of which are retained for dynamic analysis, due to cost considerations. The computational mesh consists of nearly 8 million points, including circa 130,000 points on the solid wall surfaces. The far-field boundary is located at a distance of roughly 77 reference chord lengths.

The reference flow conditions, near the design point in the current study, are an altitude of 10 km, a freestream Mach number of 0.85 and a Reynolds number based on reference chord length of 52 million. A steady-state solution is obtained

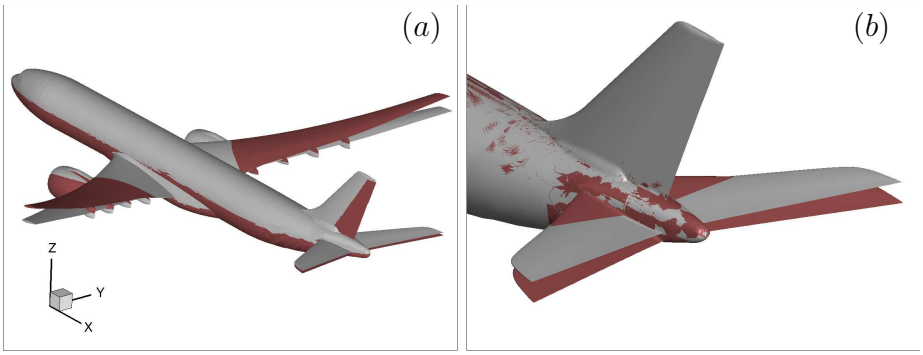

Figure 3: Representative wing-bending structural mode shape with baseline geometry in light grey in (a) and artificial horizontal tail plane mode in (b).

using an elastic trimming procedure based on Broyden's method [58], which balances lift and weight while ensuring zero pitching moment. In addition to the 94 structural modes to represent elastic deformation, an artificial trimming mode is used for rotating the horizontal tail plane, as illustrated in Fig. 3(b). During tail rotation, the junction between fuselage and tail plane is handled using the radial basis function mesh deformation technique, as described above. Trimmed angle of attack and tail angle are iteratively adjusted until the desired aerodynamic coefficients are reached with the density residual norm driven to converge seven orders of magnitude. This results in about 2.5° freestream angle of attack and a horizontal tail plane rotation of −1.5°.

The resulting steady-state surface pressure distribution is presented in Fig. 4. A strong shock along the wingspan at roughly 70% local chord length can be observed. The effects of the first wing bending mode in conjunction with torsion-dominated modes cause a decrease of sectional lift towards the wing tip. The horizontal tail plane shows a typical suction area in the vicinity of the leading edge due to the trim rotation.

We arbitrarily chose the 15 most amplified structural modes (including first wing-bending mode), identified during the steady trimming, and these are considered in the subsequent dynamic analysis. Aerodynamic responses due to simple harmonic forcing in these structural modes are sampled at 12 reduced

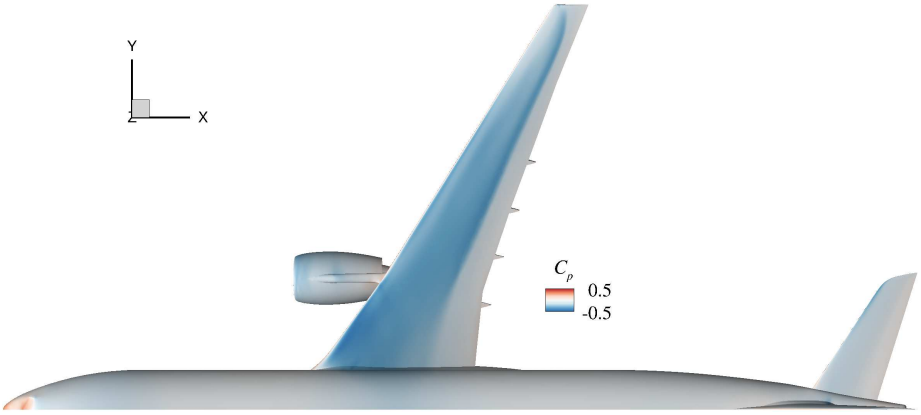

Figure 4: Surface distribution of pressure coefficient.

frequencies ω between 0 and 2, with an initial spacing of $\Delta\omega = 0.15$ up to a value of $\omega = 1.25$ and $\Delta\omega = 0.25$ thereafter. The evolution of the wind-off structural eigenvalues whilst being affected by the fluid is then traced solving Eq. (14) with a starting altitude of 50 km until the target altitude of 10 km is reached. Resulting mode traces are shown in Fig. 5. With decreasing altitude the density increases and thus the coupling between the aerodynamics and structure becomes stronger. This coupling causes all modes to deviate from the imaginary axis towards a negative real part. As expected, the configuration does not exhibit aeroelastic instability.

The impact of a pk-type approximation for aerodynamics is analysed by performing two iterations without simplifying Eq. (11). Since also the damping σ (i.e. the real part of λ) is considered in the aerodynamic coefficient matrix $Q(\lambda)$ (instead of $Q(\omega)$), while updating the eigenmodes, the method is referred to as p-type analysis to highlight the analogy to classical flutter investigations [36]. Deviations of the eigenvalues for all 15 modes are presented in Fig. 5, too. Note that a zoom is required to distinguish the approximate pk solution from the exact p-type one. Minor deviations, especially for strongly damped eigenvalues, which start interacting with aerodynamic eigenvalues, are present in the real part. This reflects the neglected influence of a damped forced oscillation.

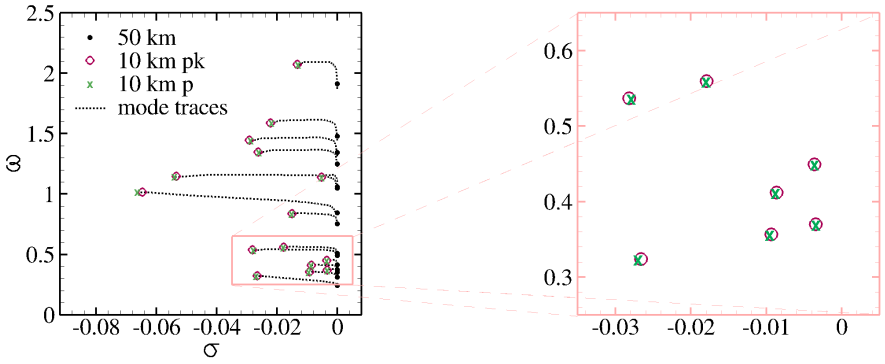

Figure 5: Evolution of eigenvalues λ during mode tracing with respect to altitude.

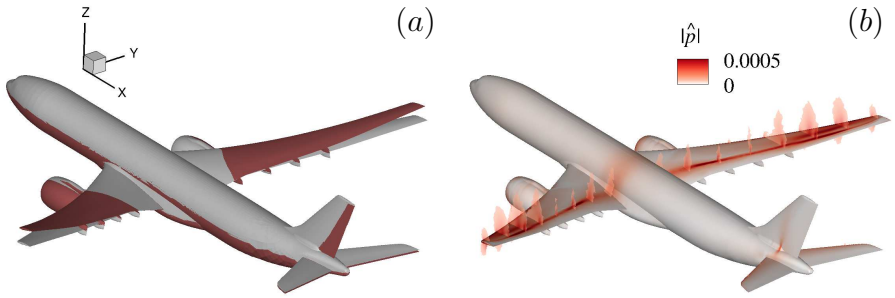

Figure 6: Visualisation of first right eigenmode $\phi_{\mathrm{EMD},1}$ showing structural deformation in (a) and magnitude of pressure component of normalised eigenvector in (b).

The fluid part of the left and right eigenvectors is computed while discarding the real part of the eigenvalue, just as for the underlying pk-type sampling. The resulting structural and fluid parts of the first right eigenmode $\boldsymbol{\phi}_{\mathrm{EMD},1}$, scaled to satisfy bi-orthonormality, are presented in Fig. 6. The structural deformation is multiplied by a factor to enhance visualisation, and it results as the linear combination of all 15 wind-off structural mode shapes, weighted by the structural degrees-of-freedom of vector $\boldsymbol{\phi}_{\mathrm{EMD},1}$, with the first eigenmode emphasising bending-dominated dynamics, cf. Fig. 3. The magnitude of pressure indicates the region in which the eigenmode has the highest influence on the pressure in the flowfield. Note that, since the whole flowfield is considered for the computation of eigenmodes, a mode affects not only the surface. Regions of high unsteady activity are a combination of strong wing deformations and already

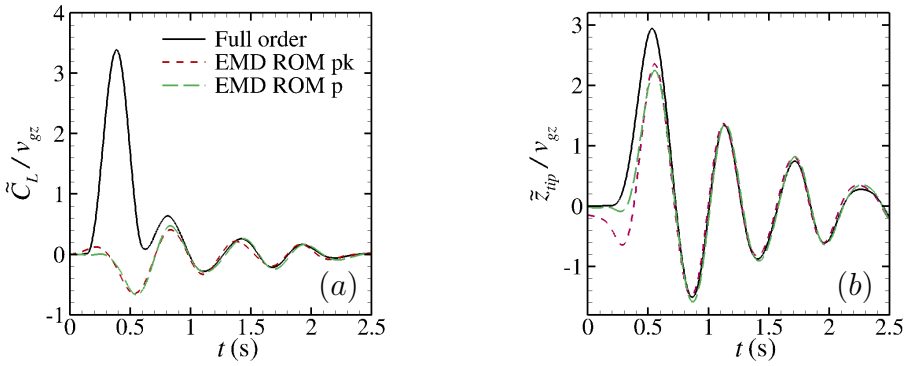

Figure 7: Gust response of EMD ROM for 1–cos gust with $L_g = 116$ m showing (a) lift coefficient and (b) wing-tip displacement, both normalised by gust amplitude.

distinct flow features in the steady-state flow field such as the outboard-wing shock location and near the leading edge on the tail plane, cf. Fig. 4.

As outlined in Section 2.3, complex conjugates of all modes are included at no additional cost, and the coupled Jacobian and gust influence matrices are projected onto the modal basis to reduce the system size from nearly 50 million to only 30 degrees-of-freedom. The generated ROM from eigenmode projection is used to investigate the gust response of the flexible aircraft. The chosen gust parameters are a gust length of $L_g = 116$ m, a vertical gust amplitude of $v_{\mathrm{gz}} = 10^{-5} \cdot U_\infty$ and a gust off-set of $x_0 = 5 \cdot L_{\mathrm{MAC}}$. The gust length is representative of a medium gust considering the certification requirements for large civil aircraft [59]. The small amplitude is imposed to ensure a dynamically linear response of the time-marching reference solution. The changes in lift coefficient and wing-tip displacement in z-direction with respect to the equilibrium solution are given in Fig. 7. Responses are normalised by the gust amplitude v_{gz} since a linearised analysis is discussed. The ROM is not capable of reproducing the lift build-up due to the gust excitation, which effectively introduces an angle-of-attack increment. However, once the gust has passed the aircraft and the aerodynamics are dominated by the damped aeroelastic response, the ROM prediction is similar to the reference. This behaviour can also be observed for the wing-tip deflection even though not as distinct.

More exact eigenmodes after two p-type iterations are used to form a ROM, too, and the gust response behaviour is analysed to investigate the influence of the pk approximation. A strong test on eigenmodes is the relation $\Psi^H A \Phi = \Lambda$, where Λ is a diagonal matrix containing the eigenvalues, which follows from bi-orthonormality. Instead of presenting these raw numbers, which do indeed confirm our methods and implementation, more illustrative results are shown in Fig. 7 not revealing major differences concerning the general trends and peak loads and deformations. This means that the influence of the pk approximation on the modal basis, for the chosen test case, is minor and not considered the root cause for discrepancies with respect to full-order results. In the following only the ROM based on the pk-equivalent mode tracing is analysed as it aligns with current practice in the aerospace sector, while keeping in mind a potential source of error due to the p-to-pk simplification.

In principle, the accuracy of responses to external excitation, such as atmospheric gusts, could be increased by enriching the modal basis with eigenmodes originating in the aerodynamic block A_{ff} of the coupled Jacobian matrix. In fact, this has been shown for a ROM based on linear potential theory, more specifically using Küssner and Wagner aerodynamics for a pitch-plunge aerofoil [16]. The problem of this approach in combination with CFD-level aerodynamics is twofold. First, the size of the Jacobian matrix directly scales with the mesh size as well as the number of conservative variables. For the case presented herein, this results in approximately 50 million degrees-of-freedom and thus determining a sufficient number of eigenvalues, and selecting the eigenvalues of interest a-posteriori, is computationally prohibitive for the time being, even though the computation of a small number of eigenmodes for such problems is possible as demonstrated for the challenge of shock-buffet stability analysis [60, 61]. Secondly, for such shift-and-invert eigenvalue computations, a region of interest must be defined a-priori which is currently not understood for gust responses. Thus, including aerodynamics-dominated eigenmodes from A_{ff} is considered not feasible and instead a subspace is approximated in the following using POD based on linearised responses of the rigid aircraft due to forced gust excitation.

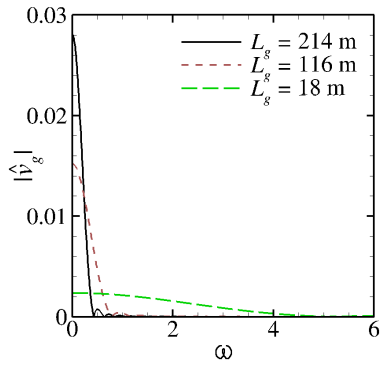

Figure 8: Magnitude of gust excitation signals in frequency domain for three gust lengths.

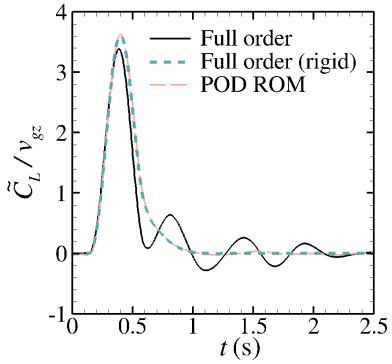

Figure 9: Change in lift coefficient for 1–cos gust with $L_g = 116$ m for POD ROM.

The gust response of the aerodynamic subsystem is sampled at 25 reduced frequencies ω between 0 and 5. Of those samples, 20 are evenly spaced between 0 and 2 and the remaining cover a range up to the value of $\omega = 5$. The relation with frequencies activated by the representative (short, medium and long) 1–cos gust signals, discussed in this work, is presented in Fig. 8. Note that the first root of the Fourier transform of the 1–cos gust signal is found at $4\pi \cdot L_{\mathrm{MAC}}/L_g$, and each subsequent root follows with an increment of $2\pi \cdot L_{\mathrm{MAC}}/L_g$. Solving Eq. (18), solutions of the entire flowfield and their corresponding complex conjugates are used as snapshots to construct a POD ROM as outlined in Section 2.4. For model reduction, all possible 49 POD modes are retained. Analysing the same gust parameters as described above, the change in lift coefficient for a

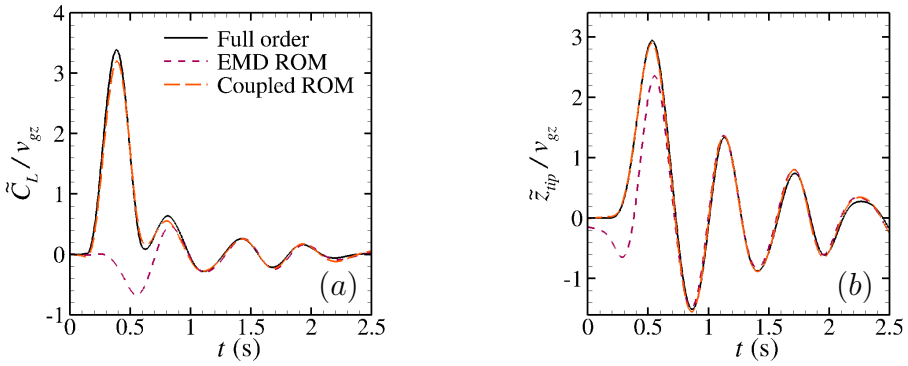

Figure 10: Response of global quantities of coupled ROM for 1–cos gust with $L_g = 116$ m showing (a) lift coefficient and (b) wing-tip displacement, both normalised by gust amplitude.

full-order, rigid aircraft gust response simulation and the POD ROM is shown in Fig. 9 with very good agreement. The full-order reference solution which accounts for structural vibration is included for convenience. Some very minor deviations are visible in the ROM response after the gust has passed the aircraft, which is a result of the sampled frequency range. A more detailed discussion of the POD ROM for this particular case, including different levels of model truncation and its influence on accuracy, has been presented previously [26].

The two modal bases are combined by using the technique outlined in Section 2.2, giving a dimension of the coupled ROM of 79 which is significantly smaller than the full system size with nearly 50 million. The coupled formulation now contains the subspace of both individual ROMs and thus is capable of predicting a coupled fluid-structure response subject to gust excitation. The resulting model is used to investigate the same gust parameters as above. The changes in lift coefficient and wing-tip displacement in z-direction with respect to the steady equilibrium solution are shown in Fig. 10. For both quantities of interest a clear improvement is observed. The ROM predicts the change in lift coefficient, while the response is dominated by gust excitation, with good agreement. Some minor differences occur around the peak value and during the transition from an aerodynamically dominated response to structurally dominated behaviour around 0.7 s. The wing-tip deflection shows an even better

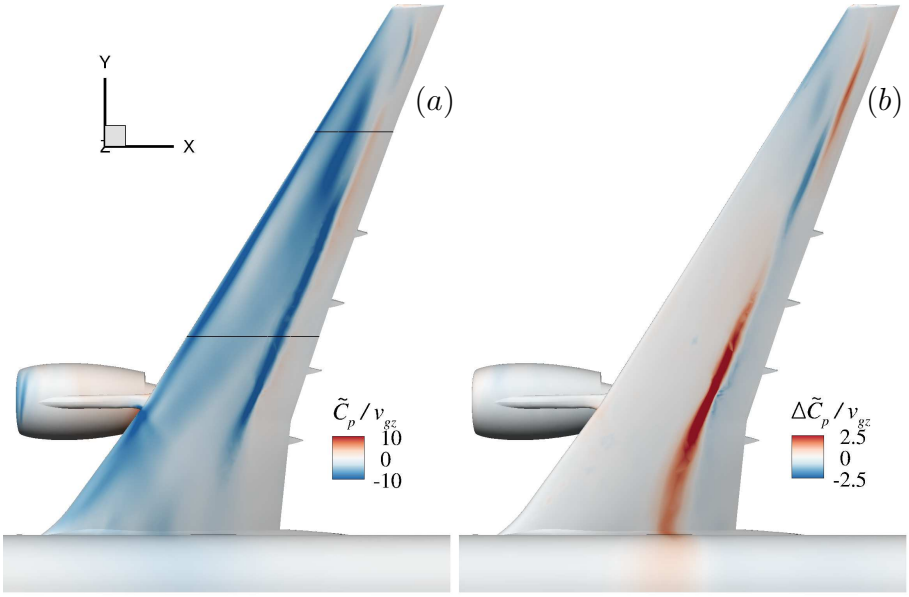

Figure 11: Change in surface pressure distribution $\widetilde{C}_p$ with respect to steady state at $C_{L,max}$ in (a) and corresponding difference $\Delta\widetilde{C}_p$ between full-order model and coupled ROM in (b) for 1–cos gust with $L_g = 116$ m. Black lines indicate extracted slices at 40% and 80% semi-span.

improvement making the predictions nearly indistinguishable.

The ROM not only offers global coefficients and structural degrees-of-freedom at greatly reduced cost but also gives access to the flow topology of the whole domain. As an example, the change in surface pressure distribution at the peak lift value with respect to the steady state is presented in Fig. 11(a). The figure shows the full-order results. Note that inspection of the corresponding reduced-order results does not give visible differences. Hence, the numerical difference between the full-order and ROM solutions is shown in Fig. 11(b). Overall good agreement is observed with some local errors in the region where the steady state exhibits non-linear features, such as the shock wave.

Based on the presented surface pressures, quantities of interest during the aircraft loads process, such as sectional loads and root wing bending moment, are readily accessible. To offer more detail, local changes in surface pressure distribution have been extracted at 40% and 80% semi-wingspan. Results are compared in Fig. 12 showing good agreement between full-order and reduced-

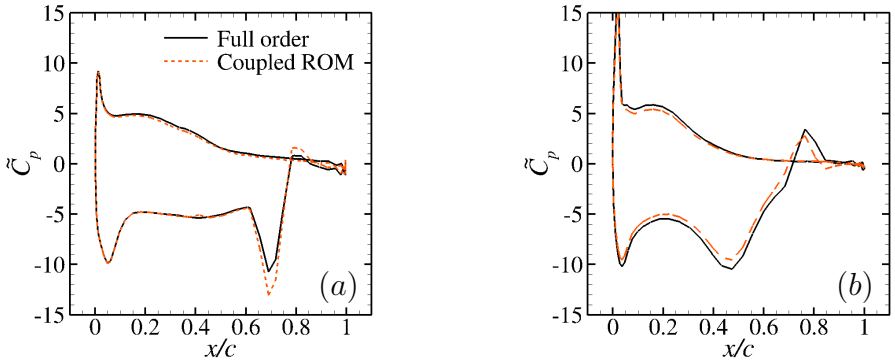

Figure 12: Change in surface pressure distribution $\widetilde{C}_p$ at $C_{L,max}$ for 1–cos gust with $L_g = 116$ m comparing full-order results and coupled ROM at selected spanwise stations; 40% semi-span in (a) and 80% semi-span in (b), as indicated in Fig. 11.

order results. Small deviations are visible around the shock location for the inboard section, whereas reference results are closely matched throughout at the outboard location. The route to integration of CFD-level aerodynamic loads in the overall aircraft design process warrants further discussion [62, 63]. For instance, traditionally, integrated loads, either through global coefficients or spanwise sectional loads (of shear, moment and torque), have been used in coupling with a simplified structural model. Our results suggest excellent integrated aerodynamic data from the reduced model approach. More sophisticated finite-element structural representations would be able to cope with distributed surface loads, and the impact of resulting local errors in the aerodynamics on the overall design needs to be scrutinised thoroughly in the future.

Once the ROM is verified for a single 1–cos gust, arbitrary gust lengths can be analysed at negligible additional computational cost. Dynamic responses for the change in lift coefficient for two representative gust lengths of $L_g = 18$ m and 214 m are provided in Fig. 13(a). These correspond to about the shortest and longest gust length, respectively, as defined by certification requirements. Excellent agreement between the reduced model and the full-order reference solutions is obtained for the longer gust, as the gust response is quasi-steady. Minor differences occur around maximum lift for the shorter gust length. Adding

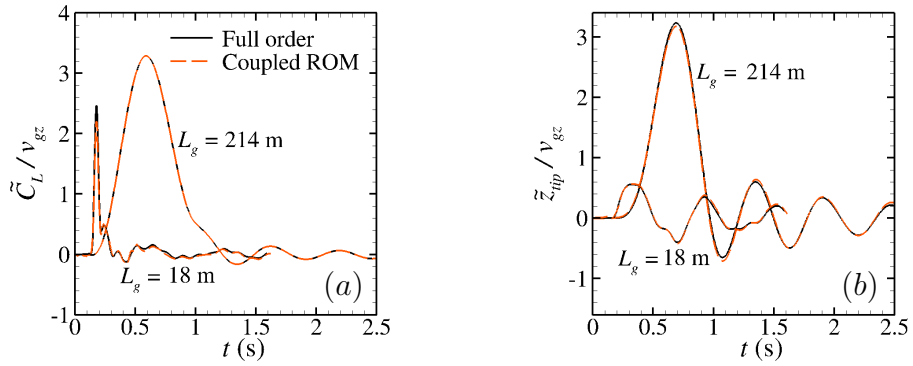

Figure 13: Gust responses of coupled ROM for 1–cos gusts with $L_g = 18$ m and $L_g = 214$ m showing (a) lift coefficient and (b) wing-tip displacement, both normalised by gust amplitude.

more samples at higher reduced frequencies for the POD ROM might improve results further for shorter gust lengths, cf. Fig. 8. Indeed, for the two longer gusts, good agreement was already found with those 20 samples going up to $\omega = 2$. The additional 5 samples to cover frequencies all the way to $\omega = 5$ helped to improve the short-gust lift prediction. In any case, the dynamic response of the wing-tip deflection in Fig. 13(b) shows good agreement throughout.

Computational cost is summarised in Tables 3 and 4. Timings were obtained on the high performance computing facility ARCHER[2] using 192 standard compute cores. Since the computational time for a time-marching non-linear 1–cos gust simulation depends on the investigated gust length, the time listed with 47 h is an average of all three presented gust responses. The CPU time of 120 h for the ROM generation includes the time needed for producing all sampling data and the subsequent coupled model construction. Solving the ROM can afterwards be done on a single core desktop computer and requires roughly 7 min, again slightly depending on the gust length of interest. It should be noted that roughly 95% of this time is needed for forming the matrix-vector product $(\Psi^H \partial \boldsymbol{R}/\partial \boldsymbol{v}_\mathrm{g}) \cdot \widetilde{\boldsymbol{v}}_\mathrm{g}$ repeatedly, since this is performed over the full-order dimension. The term in brackets only needs to be computed once though. Further

[2]Advanced Research Computing High End Resource

Offline Tasks (192 cores)	core-hours/cores
Full-order simulation (single 1–cos response)	**47 h**
Reduced-order model construction	**120 h**
a) Sampling EMD basis	107 h
b) Sampling POD basis	13 h
c) Constructing coupled ROM	$\ll$1 h

Table 3: Comparison of computational cost for aircraft case — offline task

Online Tasks (1 core)	core-hours/cores
Reduced-order model solving	**7 min**
Rebuilding global coefficients	$\ll$1 min
Rebuilding surfaces pressure distributions	$\ll$1 min

Table 4: Comparison of computational cost for aircraft case — online tasks

approximations of this term can be investigated in the future. Cost for reconstruction of global coefficients, surface pressure distributions and structural deformations is negligible. Also, as demonstrated above, the ROM, without rebuilding it, can be used to investigate a wide range of gust parameters, assuming the frequency range of interest is covered in the initial sampling. Thus, the ROM offers a speed-up compared to a full-order time-marching coupled fluid-structure simulation once more than two different sets of gust parameters are required. Based on the acceptable means of compliance [64], published together with the certification requirements, around 30 different sets of gust parameters are of interest at one flight point which results in a speed-up factor of one order of magnitude using the ROM approach presented herein.

It shall be emphasised that most of the data generated for the EMD basis construction is required already when using the frequency-domain CFD model for aerodynamic database generation and aeroelastic (flutter) stability analysis. Similar argument applies to the gust response sampling. Thus, the actual speed-up will be higher than stated, when considering the entire aircraft design and certification process and regarding the tools presented in this work as modular add-ons. In principle, our ROM formulation is a generalisation of the

conventional modal structural ROM (including projection of arbitrary aerodynamic surface data) already used for decades in industry with linear potential flow theory [34] and more recently established employing linearised CFD aerodynamics, cf. for instance [28, 65, 66]. While such established ROM is restricted to the dynamics of structural degrees-of-freedom, our formulation can deal with dominant aerodynamic modal behaviour, too, depending on choice of modal basis, and is hence better suited for edge-of-the-envelope applications. A recent example of such interesting aerodynamic challenge has been presented in the context of incipient transonic wing shock-buffet physics [60, 61], and its ramification in the aeroelastic setting is yet to be seen.

5. Conclusions

A method of model order reduction is outlined to compute coupled fluid-structure aircraft gust responses at low computational cost while preserving the physical fidelity of the underlying computational fluid dynamics solver. A 'modal decomposition and projection' philosophy is followed. Structural motion is accounted for by considering aeroelastic eigenmodes which originate from the wind-off structural degrees-of-freedom. This basis is expanded by adding proper orthogonal decomposition modes calculated from snapshots of rigid-aircraft sinusoidal gust responses to enhance the prediction accuracy during gust encounter. The linearised operator of the Reynolds-averaged Navier–Stokes equations (including the turbulence model), coupled with the structural equations, is projected onto the subspace in a Petrov–Galerkin sense. Once the reduced model is constructed, a large number of gust responses can be analysed at negligible computational cost on a local desktop computer.

The chosen practical test case is an elastically-trimmed large aircraft in transonic flow with a Mach number of 0.85 and flight Reynolds number. Global direct and adjoint eigenmodes with nearly 50 million degrees-of-freedom, to describe structural vibration, are calculated with an industry-grade multidisciplinary computational fluid dynamics package. The number of aeroelastic eigen-

modes follows industrial practice for modal structural analysis. The model based on proper orthogonal decomposition for rigid-aircraft gust encounter matches full-order reference solutions closely with a small number of modes only. The resulting combined modal basis remains small in size. Thus, a significant reduction is achieved compared to the original problem. The constructed reduced model is verified for three different gust lengths, covering short, medium and long gusts according to large aircraft certification requirements, showing excellent results throughout. Computational cost is scrutinised to evaluate the efficiency gain provided by the presented model reduction. Feasibility of rapid turnaround time using computational fluid dynamics in the industrial loads context is demonstrated, which presents a step towards the ambition of virtual aircraft design and certification and digital in-service operational support.

Acknowledgements

The authors would like to thank Airbus for providing the XRF1 test case as a mechanism for demonstration of the approaches presented in this paper. The research leading to these results was co-funded by Innovate UK, the UK's innovation agency, as part of the Enhanced Fidelity Transonic Wing project. This work used the ARCHER UK National Supercomputing Service (http://www.archer.ac.uk).

References

[1] E. Albano, W. P. Rodden, A Doublet Lattice Method for Calculating Lift Distribution on Oscillating Surfaces in Subsonic Flow, AIAA Journal 7 (2) (1969) 279–285.

[2] J. P. Giesing, W. P. Rodden, B. Stahl, Sears Function and Lifting Surface Theory for Harmonic Gust Fields, Journal of Aircraft 7 (1970) 252–255.

[3] T. Kier, Comparison of Unsteady Aerodynamic Modelling Methodologies with Respect to Flight Loads Analysis, in: AIAA Atmospheric Flight Mechanics Conference and Exhibit, 2005, aIAA 2005-6027.

[4] D. Dimitrov, R. Thormann, DLM-Correction Methods for Aerodynamic Gust Response Prediction, in: International Forum on Aeroelasticity and Structural Dynamics, 2013, iFASD Paper 2013-24C.

[5] D. E. Raveh, CFD-Based Models of Aerodynamic Gust Response, Journal of Aircraft 44 (3) (2007) 888–897.

[6] L. Reimer, M. Ritter, R. Heinrich, W. Krüger, CFD-based Gust Load Analysis for a Free-flying Flexible Passenger Aircraft in Comparison to a DLM-based Approach, in: 22nd AIAA Computational Fluid Dynamics Conference, 2015, aIAA 2015-2455.

[7] D. J. Lucia, P. S. Beran, W. A. Silva, Reduced-order modeling: new approaches for computational physics, Progress in Aerospace Sciences 40 (1-2) (2004) 51–117.

[8] R. Bartels, Developing an Accurate CFD Based Gust Model for the Truss Braced Wing Aircraft, 31st AIAA Applied Aerodynamics Conference.

[9] M. Winter, C. Breitsamter, Efficient unsteady aerodynamic loads prediction based on nonlinear system identification and proper orthogonal decomposition, Journal of Fluids and Structures 67 (2016) 1–21.

[10] R. L. Bisplinghoff, H. Ashley, R. L. Halfman, Aeroelasticity, Dover Publications, 1955.

[11] K. Taira, S. L. Brunton, S. T. M. Dawson, C. W. Rowley, T. Colonius, B. J. McKeon, O. T. Schmidt, S. Gordeyev, V. Theofilis, L. S. Ukeiley, Model Analysis of Fluid Flows: An Overview, AIAA Journal 55 (12) (2017) 4013–4041.

[12] E. H. Dowell, K. C. Hall, Modelling of fluid–structure interaction, Annual Review of Fluid Mechanics 33 (2001) 445–490.

[13] V. Theofilis, Global linear instability, Annual Review of Fluid Mechanics 43 (1) (2011) 319–352. doi:10.1146/annurev-fluid-122109-160705.

[14] K. C. Hall, Eigenanalysis of unsteady flows about airfoils, cascades, and wings, AIAA Journal 32 (12) (1994) 2426–2432.

[15] R. Florea, K. C. Hall, E. H. Dowell, Eigenmode analysis and reduced-order modeling of unsteady transonic potential flow around airfoils, Journal of Aircraft 37 (2000) 454–462. doi:10.2514/2.2619.

[16] A. Da Ronch, K. J. Badcock, Y. Wand, A. Wynn, R. Palacios, Nonlinear Model Reduction for Flexible Aircraft Control Design, in: AIAA Atmospheric Flight Mechanics Conference, 2012, aIAA 2012-4044. doi:10.2514/6.2012-4404.

[17] K. J. Badcock, M. A. Woodgate, Bifurcation Prediction of Large-Order Aeroelastic Models, AIAA Journal 48 (6) (2010) 1037–1046.

[18] M. A. Woodgate, K. J. Badcock, Fast prediction of transonic aeroelastic stability and limit cycles, AIAA Journal 45 (6) (2007) 1370–1381.

[19] S. Timme, K. J. Badcock, A. Da Ronch, Linear Reduced Order Modelling for Gust Response Analysis using the DLR-TAU Code, in: International Forum on Aeroelasticity and Structural Dynamics, 2013, iFASD Paper 2013-36A.

[20] P. Bekemeyer, S. Timme, Reduced Order Gust Response Simulation using Computational Fluid Dynamics, in: 57th AIAA/ASCE/AHS/ASC Structures, Structural Dynamics, and Materials Conference, 2016, aIAA 2016-1485.

[21] G. Berkooz, P. Holmes, J. L. Lumley, The Proper Orthogonal Decomposition in the Analysis of Turbulent Flows, Annual Review of Fluid Mechanics 25 (1993) 539 –575.

[22] J. L. Lumley, The Structures of Inhomogeneous Turbulent Flow, Atmospheric Turbulence and Radio Wave Propagation (1967) 166–178.

[23] T. Kim, Frequency-Domain Karhunen-Loève Method and Its Application to Linear Dynamic Systems, AIAA Journal 36 (11) (1998) 2117–2123.

[24] K. C. Hall, J. P. Thomas, E. H. Dowell, Proper Orthogonal Decomposition Technique for Transonic Unsteady Aerodynamic Flows, AIAA Journal 38 (10) (2000) 1853–1862.

[25] J. P. Thomas, E. H. Dowell, K. C. Hall, Three-Dimensional Transonic Aeroelasticity Using Proper Orthogonal Decomposition-Base Reduced-Order Models, Journal of Aircraft 40 (3) (2003) 544–551.

[26] P. Bekemeyer, R. Thormann, S. Timme, Rapid Gust Response Simulation of Large Civil Aircraft using Computational Fluid Dynamics, The Aeronautical Journal 121 (1246) (2017) 1795–1807.

[27] M. Förster, C. Breitsamter, Aeroelastic Prediction of Discrete Gust Loads Using Nonlinear and Time-Linearized CFD-Methods, Journal of Aeroelasticity and Structural Dynamics 3 (3) (2015) 252–255.

[28] C. Vidy, L. Katzenmeier, M. Winter, C. Breitsamter, Verification of the use of small-disturbance CFD aerodynamics in flutter and gust analysis for simple to highly complex configurations, in: International Forum on Aeroelasticity and Structural Dynamics, 2015, iFASD-2015-066.

[29] K. J. Badcock, et al., Transonic aeroelastic simulation for instability searches and uncertainty analysis, Progress in Aerospace Sciences 47 (2011) 392–423.

[30] V. Parameswaran, J. D. Baeder, Indicial Aerodynamics in Compressible Flow-Direct Computational Fluid Dynamic Calculations, Journal of Aircraft 34 (1) (1997) 131–133.

[31] R. Thormann, M. Widhalm, Linear-Frequency-Domain Predictions of Dynamic-Response Data for Viscous Transonic Flows, AIAA Journal 51 (11) (2013) 2540–2557.

[32] R. Thormann, S. Timme, Application of harmonic balance method for nonlinear gust responses, in: 2018 AIAA/ASCE/AHS/ASC Structures, Structural Dynamics, and Materials Conference, AIAA SciTech Forum, 2018, aIAA 2018-1686. doi:10.2514/6.2018-1686.

[33] E. Dowell, A Modern Course in Aeroelasticity, fifth revised and enlarged edition Edition, Springer International Publishing, 2015. doi:10.1007/978-3-319-09453-3.

[34] W. P. Rodden, Theoretical and Computational Aeroelasticity, 1st Edition, Crest Publishing, 2011.

[35] S. Timme, S. Marques, K. J. Badcock, Transonic aeroelastic stability analysis using a Kriging–based Schur complement formulation, AIAA Journal 49 (6) (2011) 1202–1213.

[36] H. J. Hassig, An approximate true damping solution of the flutter equation by determinant iteration, Journal of Aircraft 8 (11) (1971) 885–889. doi:10.2514/3.44311.

[37] P. Beran, B. Stanford, C. Schrock, Uncertainty quantification in aeroelasticity, Annual Review of Fluid Mechanics 49 (1) (2017) 361–386. doi:10.1146/annurev-fluid-122414-034441.

[38] G. Pagliuca, P. Bekemeyer, R. Thormann, S. Timme, Model reduction for gust load analysis of free-flying aircraft, in: International Forum on Aeroelasticity and Structural Dynamics, 2017, iFASD 2017-148.

[39] P. Bekemeyer, R. Thormann, S. Timme, Frequency-Domain Gust Response Simulation using Computational Fluid Dynamics, AIAA Journal 55 (7) (2017) 2174–2185.

[40] D. Amsallem, C. Farhat, On the Stability of Reduced-Order Linearized Computational Fluid Dynamics Models Based on POD and Galerkin Projection: Descriptor vs Non-Descriptor Forms, Springer International Publishing, 2014, pp. 215–233. doi:10.1007/978-3-319-02090-7_8.

[41] C. W. Rowley, Model reduction for fluids using balanced proper orthogonal decomposition, International Journal of Bifurcation and Chaos 15 (3) (2005) 997–1013. doi:10.1142/S0218127405012429.

[42] D. Schwamborn, T. Gerhold, R. Heinrich, The DLR TAU-Code: Recent Applications in Research and Industry, in: European Conference on Computational Fluid Dynamics, 2006, eCCOMAS CFD 2006.

[43] B. Stickan, J. Dillinger, G. Schewe, Computational aeroelastic investigation of a transonic limit-cycle-oscillation experiment at a transport aircraft wing model, Journal of Fluids and Structures 49 (2014) 223–241.

[44] J. Neumann, H. Mai, Gust response: Simulation of an Aeroelastic Experiment by a Fluid-Structure Interaction Method, Journal of Fluids and Structures 38 (2013) 290–302.

[45] P. R. Spalart, S. R. Allmaras, A One-Equation Turbulence Model for Aerodynamic Flows, Recherche Aerospatiale 1 (1994) 5–21.

[46] A. Jameson, W. Schmidt, E. Turkel, Numerical Solutions of the Euler Equations by Finite Volume Methods Using Runge-Kutta Time-Stepping Schemes, in: 14th Fluid and Plasma Dynamic Conference, 1981, aIAA 1981–1259.

[47] S. Langer, Agglomeration multigrid methods with implicit Runge–Kutta smoothers applied to aerodynamic simulations on unstructured grids, Journal of Computational Physics 277 (2014) 72–100. doi:https://doi.org/10.1016/j.jcp.2014.07.050.

[48] A. Michler, Aircraft control surface deflection using RBF-based mesh deformation, International Journal for Numerical Methods in Engineering 88 (2011) 986–1007.

[49] R. Heinrich, L. Reimer, Comparison of Different Approaches for Gust Modeling in the CFD Code TAU, in: International Forum on Aeroelasticity & Structural Dynamics, 2013, iFAS 2013-36B.

[50] A. Jirasek, D. M., J. Navratil, Computational Fluid Dynamics Study of Benchmark Supercritical Wing at Flutter Condition, AIAA Journal 55 (1) (2017) 153–160.

[51] N. M. Newmark, A method of computation for structural dynamics, Journal of Engineering Mechanics 85 (3) (1959) 67–94.

[52] R. Dwight, An Implicit LU-SGS Scheme for Finite-Volume Discretizations of the Navier-Stokes Equations on Hybrid Grids, DLR-FB-2005-05.

[53] M. Widhalm, R. Thormann, Efficient evaluation of dynamic response data with a linearized frequency domain solver at transonic separated flow condition, in: 35th AIAA Applied Aerodynamics Conference, AIAA AVIATION Forum, 2017, aIAA 2017-3905. doi:https://doi.org/10.2514/6.2017-3905.

[54] S. Xu, S. Timme, K. J. Badcock, Enabling off-design linearised aerodynamics analysis using Krylov subspace recycling technique, Computers and Fluids 140 (2016) 385–396.

[55] A. McCracken, A. Da Ronch, S. Timme, K. J. Badcock, Solution of linear systems in Fourier-based methods for aircraft applications, International Journal of Computational Fluid Dynamics 27 (2) (2013) 79–87. doi:10.1080/10618562.2012.750719.

[56] Y. Saad, Iterative Methods for Sparse Linear Systems, 2nd Edition, Society for Industrial and Applied Mathematics, Philadelphia, PA, 2003.

[57] C. Mettot, R. Florent, D. Sipp, Computation of eigenvalue sensitivity to base flow modifications in a discrete framework: Application to open-loop control, Journal of Computational Physics 269 (2014) 234–258.

[58] C. G. Broyden, A class of methods for solving nonlinear simultaneous equations, Mathematics of Computation (American Mathematical Society) 19 (92) (1965) 577–593.

[59] European Aviation Safety Agency, Certification Specifications for Large Aeroplanes (CS-25) (2015).

[60] S. Timme, Global instability of wing shock buffet, arXiv e-prints ArXiv:1806.07299 [physics.flu-dyn]. arXiv:1806.07299.

[61] S. Timme, Global shock buffet instability on NASA Common Research Model, in: AIAA Science and Technology Forum and Exposition (AIAA SciTech 2019), 2019, aIAA 2019-xxxx.

[62] F. Hürlimann, R. Kelm, M. Dugas, G. Kress, Investigation of local load introduction methods in aircraft pre-design, Aerospace Science and Technology 21 (1) (2012) 31–40. doi:10.1016/j.ast.2011.04.008.

[63] P. Bekemeyer, M. Ripepi, R. Heinrich, S. Görtz, Nonlinear unsteady reduced order models based on computational fluid dynamics for gust loads predictions, in: 2018 Applied Aerodynamics Conference, AIAA AVIATION Forum, 2018, aIAA 2018-3635. doi:10.2514/6.2018-3635.

[64] European Aviation Safety Agency, Certification Specifications for Large Aeroplanes Amendment 17 (CS-25) (2015).

[65] W. Weigold, B. Stickan, I. Travieso-Alvarez, C. Kaiser, P. Teufel, Linearized unsteady CFD for gust loads with TAU, in: International Forum on Aeroelasticity and Structural Dynamics, 2017, iFASD Paper 2017-187.

[66] L. Daumas, N. Forestier, A. Bissuel, G. Broux, F. Chalot, Z. Johan, M. Mallet, Industrial frequency-domain linearized Navier-Stokes calculations for aeroelastic problems in the transonic flow regime, in: International Forum on Aeroelasticity and Structural Dynamics, 2017, iFASD Paper 2017-050.